J. Fluid Mech. (2005), *vol.* 532, *pp.* 243–267.
doi:10.1017/S0022112005004052 Printed in the United Kingdom

Foam in a two-dimensional Couette shear: a local measurement of bubble deformation

By E. JANIAUD[1,2]† AND F. GRANER[3]‡

[1]Laboratoire des Milieux Désordonnés et Hétérogènes, case 78, Université Paris 6 and CNRS UMR 7603, 140 rue de Lourmel, 75015 Paris, France

[2]Université Paris 7, Denis Diderot, Fédération de Recherche FR2438 Matière et Systèmes Complexes, 2 place Jussieu, 75251 Paris Cedex 05, France

[3]Laboratoire de Spectrométrie Physique, CNRS UMR 5588 et Université Grenoble I, BP 87, F-38402 St Martin d'Hères Cedex, France

(Received 7 October 2003 and in revised form 27 November 2004)

We re-analyse experiments on a foam sheared in a two-dimensional Couette geometry. We characterize the bubble deformation by a texture tensor. Our measurements are local in time: they show two regimes, one transient and one stationary. They provide both the average and fluctuations of the anisotropy. Measurements are also local in space: they show that both the deformation and the elastic contribution to the stress field do not localize, varying smoothly across the shear gap. We can thus describe the foam as a continuous medium with elastic properties.

1. Introduction

A liquid foam exhibits 'complex' behaviour under stress: it is elastic for small deformation, plastic for large deformation, and flows at large deformation rates (Jiang *et al.* 1999; Weaire & Hutzler 1999). It is a model for the study of complex fluids: its typical length scale permits direct observation. In particular, a foam with only one bubble layer (so-called 'two-dimensional foam', Weaire & Hutzler 1999) is easy to image, and image analysis yields information on all the geometrical properties of the foam.

Debrégeas, Tabuteau & Di Meglio (2001) quasi-statically sheared a fairly dry foam in a two-dimensional Couette geometry (figure 1). They studied the velocity field and showed that it localizes in a shear band: its changes of value happen as a steep gradient on a layer much thinner than the gap, rather than over a long distance. It decreases exponentially across the gap ($r_1 - r_0$), as $\exp[-(r - r_0)/d]$. Here, r is the distance to the wheel centre, r_0 the radius of the inner wheel, r_1 the radius of the outer wheel, and $d \ll (r_1 - r_0)$ is a characteristic length comparable to one bubble diameter. Such shear-banding has been explained and numerically simulated by the combination of frozen disorder, elastic behaviour at low deformation, and local discrete bubble rearrangements, leading to an instability more likely to occur at the inner side where fluctuations are larger (Kabla & Debrégeas 2003).

What dominates the macroscopic behaviour of the material: averages or fluctuations? This question is important in the rheology of foams, as well as in other

† Present address: Foam Physics, Department of Physics, Trinity College, Dublin 2, Ireland.
‡ Author to whom correspondence should be addressed: graner@ujf-grenoble.fr

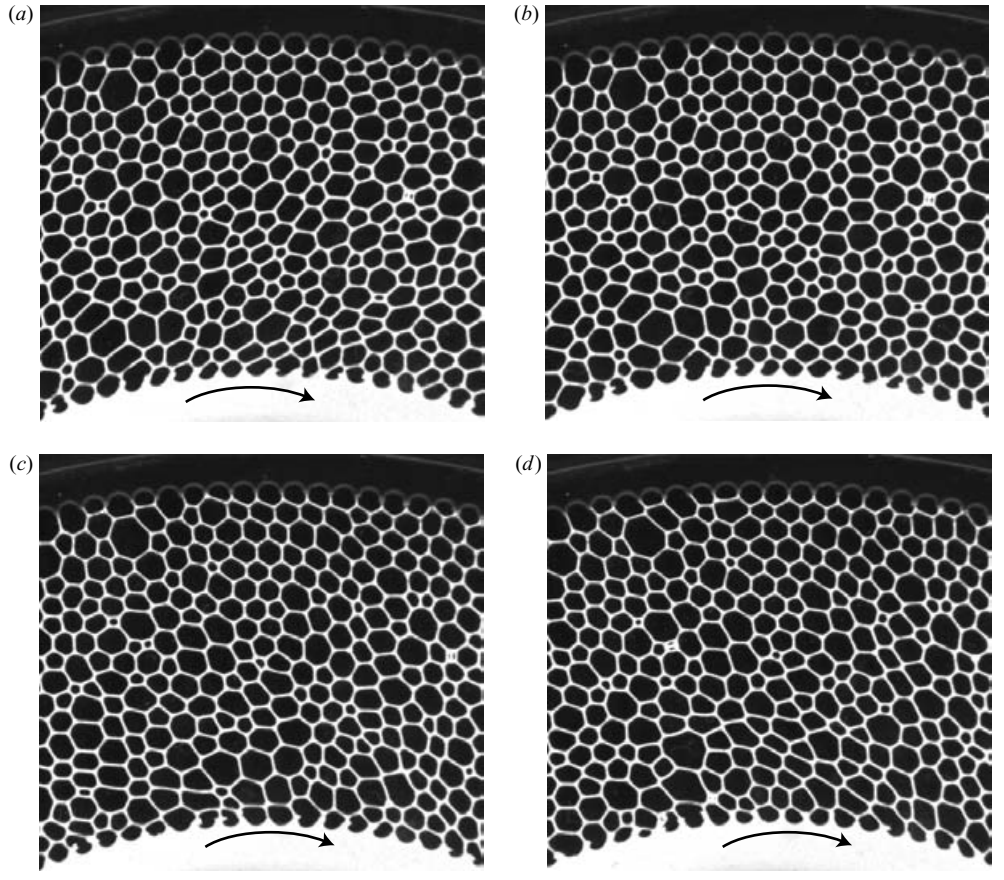

FIGURE 1. Run 1 (transient regime): foam under steady quasi-static shear in a Couette geometry. Pictures of the foam correspond to different values of applied shear strain γ. (*a*) 0, immediately after switching from counterclockwise to clockwise rotation; (*b*) 0.15; (*c*) 0.5, when the inner boxes have reached the yield strain (see figure 5); and (*d*) 7.6, well into the stationary regime. The cross-component $r\theta$ of the texture tensor, defined in (3.11), is (*a*) positive, (*b*) zero, (*c*) negative, and (*d*) stationary.

disordered materials. Briefly, if the signature of fluctuations averages out at large scales, a 'thermodynamical limit' exists in which the average dominates; a constitutive equation relating the stress and strain fields can then describe the material as a continuous medium (like a solid or a liquid). If the fluctuations have the same order of magnitude as the average at all scales, they can dominate the physical behaviour, which need not correspond to any continuous medium. Whenever the fluctuations dominate, we can ask whether they correlate (leading to large stress drops) or have a white spectrum. The answer need not be the same for different materials (say, foam and granular materials) nor for different quantities (say, velocity and deformation).

Similarly, the existence and origin of localization raise different questions: the effect of boundary conditions, the respective roles of strain and strain rate, the precise role of fluctuations, the differences between various (disordered) materials, the distinction between sharp (Coussot *et al.* 2002) or exponential (Debrégeas *et al.* 2001) decreases, the dimension of space (two-dimensional or three-dimensional), and even the field itself (velocity or deformation).

We would like to extract additional physical information, beyond the velocity field. Most suggestions for quantifying statistically the anisotropy and the deformation of the internal structure of the foam, that is, the bubble wall network, are based on scalar quantities (Elias *et al.* 1999). Since the deformation encompasses information on both anisotropy and orientation, it is actually a tensor (Landau & Lifschitz 1986; Alexander 1998). Recent suggestions of possible tensorial descriptions based on bubble details are promising (Reinelt & Kraynik 2000; Ball & Blumenfeld 2002; Kraynik, Reinelt & van Swol 2003; Blumenfeld 2004). Here, we use the 'texture tensor' (equation (3.11)), which has the following advantages (Aubouy *et al.* 2003): (i) it is purely geometrical, independent of stresses and forces; (ii) it applies to both small and large numbers of bubbles; (iii) it is local in time and space (Jiang *et al.* 2000), so it can characterize a subregion of the foam; (iv) it applies to disordered or ordered, two-dimensional or three-dimensional materials, in elastic, plastic or fluid regimes.

The plan of this paper is as follows. Section 2 reviews the original experimental set-up, and our image analysis protocol. The theoretical section, § 3, reviews the definitions and measurements of stress, texture and strain tensors; it can be read separately. Section 4 presents our analyses of experiments. Section 4.1, resolved in both time and space, studies the transient regime before a stationary flow is established. Section 4.2, resolved in space but averaged in time, shows that in stationary flow, both the bubble anisotropy and the elastic contribution to the deviatoric stress field vary smoothly across the Couette gap; they do not localize near the inner rotating wheel. Section 4.3, again resolved in time, shows that in stationary flow, the fluctuations are larger near the inner wheel. In § 5, we discuss whether we can describe the foam as a continuous medium with elastic properties.

2. Materials and methods

2.1. *Experiments*

G. Debrégeas generously provided experimental data obtained in two different runs. For experimental details see Debrégeas *et al.* 2001. Briefly, the set-up consists of an inner shearing wheel and an outer fixed one, with no-slip conditions due to tooth-shaped boundaries (tooth depth: radius 1.2 mm). The foam is confined between two transparent plates separated by $h = 2$ mm spacers (figure 2*d*); this foam thickness is smaller than the distance between bubble centres (see below), enforcing a single layer of bubbles (Cox, Weaire & Vaz 2002). The fluid fraction, measured by the weight of water introduced in the cell, is $\Phi = 5.2\,\%$. The bubble size dispersity is $\sim 30\,\%$, enough to prevent crystallization. Coarsening and size sorting under shear are negligible during the experiment. A CCD digital camera records the position and the shape of the bubbles.

The inner wheel rotates slowly enough ($V_{wheel} = 0.25\,\mathrm{mm\,s^{-1}}$) that the flow is well in the quasi-static regime: the foam passes through a succession of equilibrium states. All averaged static physical quantities, like the elastic strain or stress, remain the same if the applied shear rate $V_{wheel}/(r_1 - r_0)$ varies. Kinetic quantities, like the velocity field, the rate of T1 processes (neighbour swapping), and the input power and dissipation, scale as the shear rate. This scaling is typical of solid-like friction (only at higher velocity does the foam exhibit a fluid-like friction, when the input power and dissipation scale like the square of the shear rate). As required for comparison to other experiments, we thus express all results as a function of the total applied shear

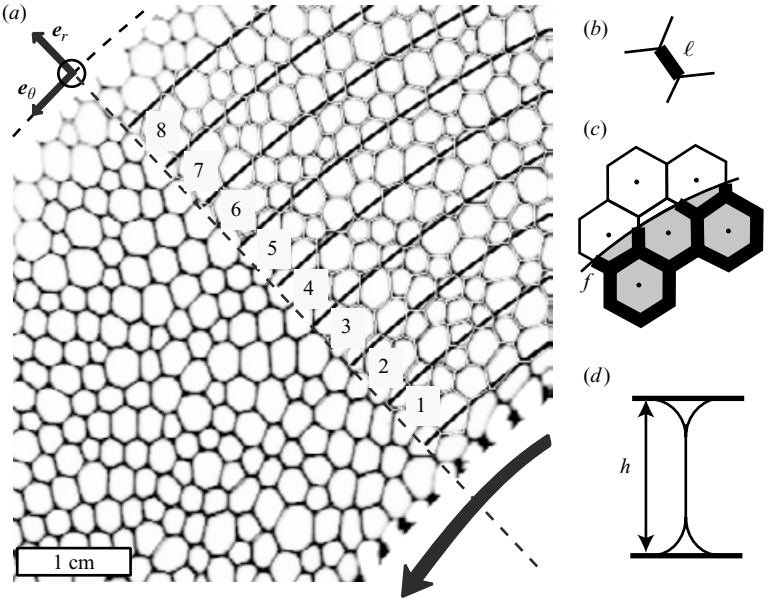

FIGURE 2. Run 2 (stationary flow): image analysis and notations. (*a*) *Bottom left:* top view of the original experiment by Debrégeas *et al.* (2001), rotating counterclockwise. *Top right:* image analysis. The reconstructed network of vertices linked by vectors (white) and the boundaries of the 8 equi-spaced concentric circular boxes used as representative volume elements (RVE) for spatial analysis (black circular arcs) are superimposed on the snapshot of the experiment. We exclude the regions near both wheels, where the bubbles are not entirely visible. (*b*) We denote by $\boldsymbol{\ell}$ the vector linking both vertices of a given wall. (*c*) If one of these vertices is outside of the box (defined in (*a*), top right), we denote by $f \in [0, 1]$ the fraction of the bubble wall length inside the box; $f = 0$ if the wall is entirely outside, $f = 1$ if it is entirely inside. (*d*) Side-view sketch of a vertical bubble wall cross-section, between two horizontal glass plates.

strain:

$$\gamma = \frac{V_{wheel}\, t}{r_1 - r_0}. \tag{2.1}$$

Note that γ is proportional to time t, not to the local shear in each box.

Run 1 (unpublished data) contains a transient regime. To prepare the foam, the inner disk is rotated counterclockwise, until a stationary regime is reached. Then, at an arbitrary time, chosen as the origin ($t = \gamma = 0$), the shear direction is switched to clockwise (figure 1), the experiment begins and 500 pictures are recorded. The $r\theta$ components of the deformation thus switch from positive to negative (figure 3). Each picture shows 200 bubbles, in an angular sector of the experimental cell (figure 1). The average distance between the centres of mass of neighbouring bubbles is 3.0 mm, with a standard deviation of ± 0.5 mm, corresponding to a mean bubble wall length of $\langle \ell \rangle = 1.7$ mm. The internal radius is $r_0 = 71$ mm (same for both runs) and the external radius is $r_1 = 112$ mm (different for each run). Thus, $\gamma = 1$ corresponds to a wheel displacement of $V_{wheel}\, t = r_1 - r_0 = 41$ mm, i.e. 15–20 bubble diameters.

Run 2 (published in Debrégeas *et al.* 2001) focuses on the stationary regime. The preparatory rotation is clockwise. Then, at an arbitrary time, chosen as the origin ($t = \gamma = 0$), it is switched to counterclockwise (figure 2). Pictures are recorded only after a full 2π-turn, corresponding to $\gamma = 8$; the $r\theta$ components of the deformation are thus positive (figure 6). A quarter of the Couette cell is filmed, with 700 bubbles

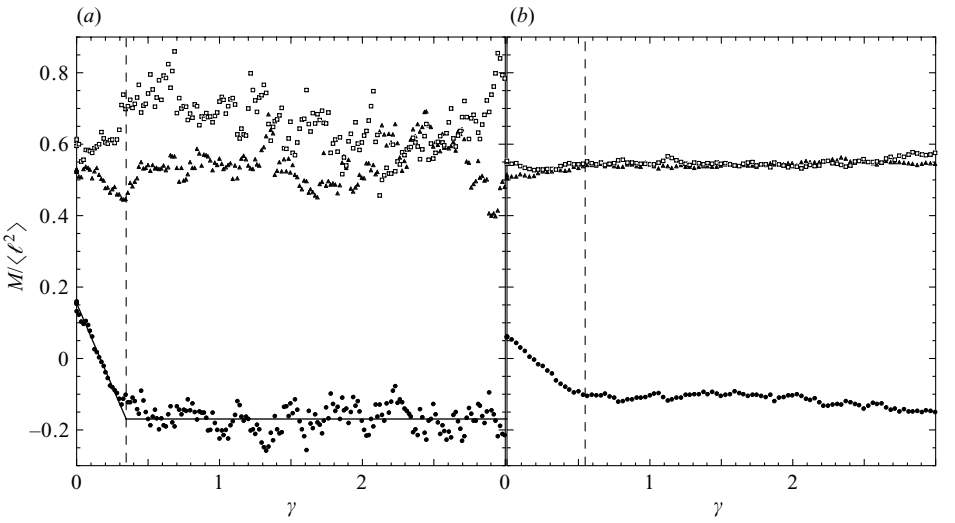

FIGURE 3. Run 1 (transient regime): texture tensor $\boldsymbol{M}$ versus the applied shear strain γ. The components of $\boldsymbol{M}$ defined in (3.11) and measured from the first 200 images (▲, M_{rr}; □, $M_{\theta\theta}$; ●, $M_{r\theta}$) are expressed in units of the average length of the bubble wall, $\langle \ell^2 \rangle$. (*a*) Innermost box (number 1): each point represents one image; (*b*) outermost box (number 8): for clarity, we show only every second image. The vertical dashed line marks the cross-over γ_Y between the transient and stationary regimes, defined by the intersection between the straight line and the zero slope line fitting $M_{r\theta}$ in the transient and stationary regimes, respectively (solid lines in (*a*)).

in each picture. To improve the statistics, the camera is then displaced to record the four quarters successively; 2000 pictures are obtained as four 500-image movies. Data are measured and averaged over the four quarters of the foam. The average distance between the centres of mass of neighbouring bubbles is 2.4 mm, with a standard deviation of ± 0.4 mm, corresponding to a mean bubble wall length of $\langle \ell \rangle = 1.4$ mm. The internal radius is $r_0 = 71$ mm (same for both runs) and the external radius is $r_1 = 122$ mm (different for each run). Thus, $\gamma = 1$ corresponds to a wheel displacement of 51 mm, i.e. 20–25 bubbles diameters.

2.2. *Image analysis*

We analyse the images using a home-made extension module to the public software NIH-Image. We threshold the image, and skeletize the bubble walls to a one-pixel thickness. We identify the points where three walls meet ('vertices'). We replace each wall by the vector $\boldsymbol{\ell}$ linking its vertices (white lines in figure 2*a*, top right).

To respect the symmetry of the Couette cell, this wall vector $\boldsymbol{\ell}$ (figure 2*b*) is expressed in local polar coordinates (r, θ) (figure 2*a*). This neglects the variation of the polar referential between both its end points. This assumption is correct as long as $\ell \ll r$.

For the same reason, we choose equi-spaced orthoradial, circular boxes (figure 2*a*, top right) to divide the foam and measure the deformation using spatial averages to improve the statistics. In the quasi-static regime, the bubble deformation remains very small and barely visible by eye. After trying various box sizes, we chose 8 boxes as a compromise between the quality of the statistics and the level of visible details.

For Run 1, each box is $2.7\langle \ell \rangle$ wide, and box number i is at position $r_1^i = r_0 + [0.4 + 2.7(i - 0.5)]\langle \ell \rangle$. The number of bubbles in each box grows linearly, typically from 17 bubbles in the first box, to 32 in the eighth box.

For Run 2, $r_2^i = r_0 + [2.8 + 3.1(i - 0.5)]\langle \ell \rangle$. Owing to the shape of the pictures (figure 2*a*), the number of bubbles first increases with i (from typically 105 bubbles in the first box), then decreases (to 41 in the eighth box).

3. Definitions and measurements of deviatoric elastic stress and strain

3.1. *Capillary contribution to the stress*

3.1.1. *Theoretical definition*

In fluid foams, the three main contributions to stress $\boldsymbol{\sigma}$ are the capillary term $\boldsymbol{\sigma}^{cap}$ due to the tension of the liquid walls, the pressure of the gas within each bubble, and the viscous dissipation. In what follows, the 'deviatoric' part of the capillary stress refers to the traceless tensor, i.e. $\boldsymbol{\sigma}^{cap} - \mathrm{Tr}(\boldsymbol{\sigma}^{cap})\,\boldsymbol{I}/2$, where $\boldsymbol{I}$ is the identity tensor in two dimensions. It consists in the shear stress $\sigma_{r\theta}^{cap}$ and the normal stress difference $\sigma_{rr}^{cap} - \sigma_{\theta\theta}^{cap}$.

In the extreme 'wet foam' limit $\Phi \sim 1$, bubbles are well separated from each other. The capillary contribution in a representative volume element (RVE) V which contains N bubbles with surface tension Γ is (Rosenkilde 1967; Batchelor 1970):

$$\left.\begin{aligned} \boldsymbol{\sigma}^{cap} &= \frac{\Gamma}{V} \sum_{S \in V} \oint_S (\boldsymbol{I} - \boldsymbol{n} \otimes \boldsymbol{n})\, \mathrm{d}s, \\ \sigma_{ij}^{cap} &= \Gamma \frac{N}{V} \left\langle \oint_S (\delta_{ij} - n_i n_j)\, \mathrm{d}s \right\rangle_V . \end{aligned}\right\} \tag{3.1}$$

Here, N/V is the density of bubbles; S is the surface of each bubble; $\boldsymbol{n}$ is the unit vector normal to the surface element $\mathrm{d}s$; and $\langle . \rangle_V$ is the average over bubbles in V.

In the other extreme, 'dry foam' limit $\Phi \ll 1$, pairs of bubble surfaces merge into a film with surface tension 2Γ. The capillary contribution is (Khan & Armstrong 1986; 1987; Reinelt & Kraynik 2000; Kraynik *et al.* 2003):

$$\boldsymbol{\sigma}^{cap} = \frac{2\Gamma}{NV} \oint_S (\boldsymbol{I} - \boldsymbol{n} \otimes \boldsymbol{n})\, \mathrm{d}s + O(\Phi^2). \tag{3.2}$$

The correction of order Φ^2 is a contribution of the integral over the surface S of its mean curvature (Mecke & Stoyan 2002). Since the mean curvature is mostly concentrated in bubble edges ('Plateau borders'), this contribution is physically equivalent to the recently identified line tension which affects the bubble edges (Kern & Weaire 2003; Géminard *et al.* 2004).

3.1.2. *Operational definition in two dimensions*

A true two-dimensional foam has an interesting property: at equilibrium, or in a quasi-static regime, the coarse-grained Laplacian of the pressure is zero (Graner *et al.* 2001; Graner 2002). The small-scale fluctuations of bubble pressures, according to bubble side numbers, average out to zero at large scales (Weaire & Hutzler 1999). In the present Couette geometry, where no large-scale pressure gradient exists, pressure does not vary significantly (Weaire *et al.* 2004). Hence, in-plane curvatures remain much smaller than the inverse of bubble sizes. They contribute to the stress through their algebric average (not their second moment), which is small along any path within the foam: curvatures are counted positively if the path crosses the wall from the concave side (Graner 2002). They thus induce only a negligible correction to the deviatoric capillary stress, with respect to straight walls (Asipauskas *et al.* 2003).

However, adapting the definition in (3.2) to measure deviatoric capillary stress fields in bubble monolayers requires care. In the present case, the curvature radius in the third dimension, not visible in images, is smaller or equal to the half-distance between plates (figure 2*d*). Its inverse, namely the curvature in the third dimension, is larger than the curvature visible in the image. This case is thus intermediate between two limiting bubble monolayers: bubble rafts, and Langmuir foams.

In bubble rafts, stress has already been measured, in a circular Couette geometry, by mechanical measurements of the force at the boundaries (Pratt & Dennin 2003), or indirectly by local measurements of bubble ellipticity (Ybert & di Meglio 2002). Since bubble top surfaces are curved (they are approximately spherical caps), direct local measurements of stress are difficult.

At the other extreme, Langmuir foams are one molecule thick: their aspect ratio is of the order of nanometres divided by centimetres, with no well-defined curvature in the third dimension. They are thus probably the closest approximation to a true two-dimensional foam (as long as three-dimensional viscosity effects remain negligible), and capillary stress fields can be measured as described below (equation (3.5)) (Courty *et al.* 2003).

In the present case, for a single layer of bubbles (Cox, Weaire & Vaz 2002) in the quasi-static regime, the dry part of the film remains vertical (figure 2*d*). By symmetry, we can assume that the curvatures on both sides of a film are almost opposite, so that their effects almost cancel each other. We thus neglect the effect of curvature in the third dimension.

We further simplify (3.2) using two approximations. First, although strictly speaking it applies to closed surfaces (complete surfaces of bubbles), we extend it to averages on open surfaces (walls between bubbles), assuming that any possible non-compensated term (due for instance to bubbles at the foam boundary) has a negligible contribution to the average (Kraynik *et al.* 2003). Secondly, on closed surfaces in two dimensions, the integral of the mean curvature only contributes a constant, so that the $O(\Phi^2)$ term need not be considered here; in what follows, on open surfaces, we again neglect the contribution of possible non-compensated terms.

Finally, (3.2) simplifies to an expression which has already been used (but not always justified) for various types of bubble monolayers (Weaire & Hutzler 1999; Asipauskas *et al.* 2003; Courty *et al.* 2003; Kabla & Debrégeas 2003):

$$\boldsymbol{\sigma}^{cap} = \frac{1}{V} \sum_{\boldsymbol{\ell}} f(\lambda \hat{e} \otimes \boldsymbol{\ell}). \tag{3.3}$$

Here (figure 2) the two-dimensional RVE V is a surface area; the $\boldsymbol{\ell}$s are the chords linking two connected vertices, approximating bubble walls; f is the fraction of the wall length contained in V; $\hat{e} = \boldsymbol{\ell}/\ell$ is the unit vector tangent to $\boldsymbol{\ell}$. The line tension λ is equal to Γh multiplied by a geometric constant which depends on Φ (figure 2*d*): it varies from 2 for a dry foam (two flat interfaces of length h) to π for a wet foam (two half-circles of diameter h).

3.1.3. *Comments on this definition*

Equation (3.3) is analogous to the expression for the elastic stress in a (two-dimensional or three-dimensional) network with a density ρ of links $\boldsymbol{\ell}$ undergoing two-body interactions with tensions $\boldsymbol{\tau}$ (Kruyt 2003):

$$\boldsymbol{\sigma}^{cap} = \rho \left\langle \boldsymbol{\tau} \otimes \boldsymbol{\ell} \right\rangle_V . \tag{3.4}$$

In the continuum limit, the average $\langle . \rangle_V$ is the average of the wall probability distribution function, and this expression for the stress is exactly the same (see for instance Kruyt (2003) or the Appendix of Aubouy *et al.* (2003)) as the classical definition based on the links crossing the boundaries of V (Landau & Lifschitz 1986). This equivalence validates *a posteriori* our application of (3.2) to open surfaces. In practice, experimental data have a finite size: the number of links used in the calculation, and so the signal/noise ratio of the resulting measurement (Asipauskas *et al.* 2003), is much larger if we use all links in V, rather than only the links crossing its boundaries.

Equation (3.4) shows that, in a network of points which interact through a pairwise potential, we can measure the stress from an image if we know the expression for the two-points force law $\boldsymbol{\tau} = \boldsymbol{\tau}(\boldsymbol{\ell})$ explicitly (for instance Lennard–Jones, or harmonic).

For quasi-static two-dimensional foams (equation (3.3)), all tensions have the same modulus λ; hence, $\boldsymbol{\tau}(\boldsymbol{\ell}) = \lambda \hat{e}$. The image provides $\boldsymbol{\sigma}^{cap}/\lambda$, which is enough for our purposes:

$$\left.\begin{aligned} \frac{\boldsymbol{\sigma}^{cap}}{\lambda} &= \rho \, \langle \hat{e} \otimes \boldsymbol{\ell} \rangle_V \, , \\ \frac{\sigma_{ij}^{cap}}{\lambda} &= \rho \left\langle \frac{\ell_i \ell_j}{\ell} \right\rangle_V . \end{aligned}\right\} \tag{3.5}$$

Here, ρ is the area density of bubble walls: the number of bubble walls in V weighted by f, divided by V; $\langle . \rangle_V$ is the average over the walls in V, also weighted by f.

3.2. *Status of the elastic strain tensor*

3.2.1. *Macroscopic definition of the elastic strain*

A macroscopic definition of elastic strain (Macosko 1994; Farahani & Naghdabadi 2000) is usually a function of the *deformation gradient* $\boldsymbol{F}$:

$$\left.\begin{aligned} \boldsymbol{F} &= \left(\frac{\partial \boldsymbol{x}}{\partial \boldsymbol{x}^0} \right)^t = (\nabla \cdot \boldsymbol{x}), \\ F_{ij} &= \frac{\partial x_i}{\partial x_j^0}, \end{aligned}\right\} \tag{3.6}$$

where $\boldsymbol{x}$ is the current position of a point initially at position $\boldsymbol{x}^0$. This deformation gradient $\boldsymbol{F}$ coincides with the identity $\boldsymbol{I}$ in a solid translation, and has a determinant 1 in a volume-conserving transformation.

From $\boldsymbol{F}$, we can define two symmetric tensors $\boldsymbol{U}$ and $\boldsymbol{V}$ through a rotation $\boldsymbol{R}$ (Phan-Thien 2002):

$$\boldsymbol{F} = \boldsymbol{R}\boldsymbol{U} = \boldsymbol{V}\boldsymbol{R}. \tag{3.7}$$

They are called the *right* and *left stretch tensors*. They coincide with the identity $\boldsymbol{I}$ in a solid transformation (translation and rotation), and also have a determinant 1 in a volume-conserving transformation.

In turn, they determine a *right* and a *left deformation* (or Cauchy–Green) tensor, respectively (Phan-Thien 2002):

$$\left.\begin{aligned} \boldsymbol{C} &= \boldsymbol{F}^t \boldsymbol{F} = \boldsymbol{U}^2, \\ \boldsymbol{B} &= \boldsymbol{F}\boldsymbol{F}^t = \boldsymbol{V}^2. \end{aligned}\right\} \tag{3.8}$$

They too are symmetric, coincide with the identity $\boldsymbol{I}$ in a solid transformation (translation and rotation), and have a determinant 1 in a volume-conserving transformation.

Finally, a *strain measure tensor* $\boldsymbol{E}$ is for instance equal to $(\boldsymbol{B}-\boldsymbol{I})/2$, $(\boldsymbol{C}-\boldsymbol{I})/2$, or more generally to one of the Seth–Hill strain measure tensors based on the successive powers of $\boldsymbol{U}$ or $\boldsymbol{V}$:

$$\left.\begin{aligned} \boldsymbol{E}^{(m)} &= \frac{\boldsymbol{U}^m-\boldsymbol{I}}{m}, \\ \text{or}\quad \boldsymbol{E}^{(m)} &= \frac{\boldsymbol{V}^m-\boldsymbol{I}}{m}, \end{aligned}\right\} \tag{3.9}$$

where m is a positive or negative integer (Farahani & Naghdabadi 2000). They all tend towards the linear elasticity definition (the gradient of the displacement field) in the limit of infinitesimal transformation.

The particular case of $m=0$ corresponds to the logarithm-based definition (Hoger 1987) and generalizes the Hencky strain tensor (Tanner & Tanner 2003) to arbitrary deformations:

$$\left.\begin{aligned} \boldsymbol{E}^{(0)} &= \log \boldsymbol{U} = \tfrac{1}{2}\log \boldsymbol{C}, \\ \text{or}\quad \boldsymbol{E}^{(0)} &= \log \boldsymbol{V} = \tfrac{1}{2}\log \boldsymbol{B}. \end{aligned}\right\} \tag{3.10}$$

This *true strain tensor* $\boldsymbol{E}^{(0)}$ correctly quantifies both volume-invariant deformations (which appear as traceless strain tensors) and dilations (which appear as the logarithm of the volume, as, for example, in gases).

Constitutive equations of a material, that is stress–strain relations, can use either of these tensors; some arguments favour right tensors (Larson 1997; Farahani & Naghdabadi 2000) while other favour left ones (Macosko 1994).

3.2.2. *Micromechanical definitions of elastic strain*

A microscopic definition of elastic strain (Kruyt & Rothenburg 1996; Liao *et al.* 1997; Alexander 1998; Zimmerman 1999; Ball & Blumenfeld 2002; Goldhirsch & Goldenberg 2002; Aubouy *et al.* 2003; Kruyt 2003; Blumenfeld 2004) adopts a different point of view: it constructs the macroscopic elastic strain from the positions of individual 'sites' (i.e. atoms, grains, or vertices of a network), just as stress is constructed from individual forces, see (3.4).

For instance, Zimmerman (1999) considers elastic deformations of two-dimensional or three-dimensional ordered atomic crystals. He constructs separately the stress (from atomistic potentials) and the elastic strain (from displacements). He shows that, in the ordered cases he considers, his strain yields a continuum-mechanics limit identical to that derived from the Cauchy–Green tensor.

Kruyt (2003) expands the analysis he used in a series of papers with Rothenburg, which, for instance, predicted the elastic moduli of disordered or ordered two-dimensional granular materials (Kruyt & Rothenburg 2002). He constructs separately the stress from individual forces (obeying equilibrium conditions) and the elastic strain from individual displacements (obeying geometric compatibility conditions) small enough to avoid rearrangements (Kruyt 2003).

Goldhirsch & Goldenberg (2002) rewrite elasticity theory on a microscopic basis, take the continuous limit, and show its compatibility with classical elasticity, including the energetics and conjugation relations (Goldhirsch & Goldenberg 2002). In

particular, they show that their definition of elastic strain is better than those based, for instance, on fits of the displacements to a macroscopic strain field (Liao *et al.* 1997) and that, even for granular materials, microscopic fluctuations progressively average out when going to macroscopic scales.

3.3. *Extension to plastic and fluid regimes*

Macroscopic and micromechanic elastic strain tensors become difficult to define after the first topological rearrangement. They finally lose their meaning after a few rotations of the Couette-cell inner wheel, and mathematical singularities appear. This breakdown of formalism is counterintuitive; experimentally, the mechanical behaviours of elasto-plasto-viscous materials do not appear to change discountinuously.

We need to treat the (even large) elastic deformation, independently from the flow involving rearrangements of the connections between neighbouring sites (changes in network topology). The total applied shear strain decomposes into plastic and elastic strains. The plastic strain is much larger, since it increases linearly with time (its derivative, corresponding to the velocity gradient, is constant in steady flow). The elastic strain is much smaller: here, in steady flow, it remains constant; but it is physically important, because it characterizes the current state of the foam.

We use below the approach of Aubouy *et al.* (2003), which consists of three steps. It first characterizes the current state of the material by a 'texture' (or 'fabric') tensor $\boldsymbol{M}$, built from statistical averages over microscopic positions, which exists in all regimes. It then defines a reference state characterized by a reference tensor $\boldsymbol{M}_0$. It finally constructs the elastic strain by a comparison of both tensors. We now review these definitions.

3.3.1. *Texture tensor*

The pattern of the walls in a region of the foam can be statistically characterized by the local *texture tensor* $\boldsymbol{M}$ (Aubouy *et al.* 2003). In two-dimensions, it is written as (again with averages weighted by f):

$$\left.\begin{aligned} \boldsymbol{M} &= \langle \boldsymbol{\ell} \otimes \boldsymbol{\ell} \rangle_V , \\ M_{ij} &= \langle \ell_i \ell_j \rangle_V = \left\langle \begin{pmatrix} \ell_r^2 & \ell_\theta \ell_r \\ \ell_r \ell_\theta & \ell_\theta^2 \end{pmatrix} \right\rangle_V . \end{aligned} \right\} \tag{3.11}$$

It accounts for the direction and length ℓ of the walls; however, since the symmetry $\boldsymbol{\ell} \to -\boldsymbol{\ell}$ does not affect the pattern, the orientation of $\boldsymbol{\ell}$ plays no role.

The diagonal components M_{rr} and $M_{\theta\theta}$ of this tensor are both of order $\langle \ell^2 \rangle$. Conversely, the off-diagonal component $M_{r\theta} = M_{\theta r}$ (the tensor is symmetric), and the difference $M_{rr} - M_{\theta\theta}$, together characterize the anisotropy: they are both much smaller than $\langle \ell^2 \rangle$. They vanish when the foam is isotropic; in which case $\boldsymbol{M} = (\langle \ell^2 \rangle / 2)\boldsymbol{I}$ is proportional to $\boldsymbol{I}$, and only encodes the r.m.s. wall length. Hence the tensor $\boldsymbol{M}$ has two strictly positive eigenvalues, also of order $\langle \ell^2 \rangle$, the larger being in the direction in which bubbles elongate. It thus quantifies the average size, as well as the anisotropy direction and amplitude, of the network consisting of the bubble vertices (figure 2*a*, top right). In a stationary regime, it is constant, as are all averaged physical quantities.

3.3.2. *Reference state*

At any time, the current state of the foam corresponds to a current reference state, namely the state that the foam reaches after relaxation (Porte, Berret & Harden 1997). This reference state defines the *reference texture tensor* $\boldsymbol{M}_0$. It varies with time; but in a stationary regime, it is constant, as are all averaged physical

quantities including $\boldsymbol{M}$. The reference state is not necessarily equal to the initial state (Porte *et al.* 1997).

In the present experiment, letting the inner wheel rotate back freely is difficult, so that in practice we do not have direct access to a reference state. However, we do not need microscopical details to estimate $\boldsymbol{M}_0$: it suffices to make a physical approximation on the average properties of the foam at rest. We chose below to assume that the reference state is statistically isotropic. We thus approximate $\boldsymbol{M}_0$ by $M_0\,\boldsymbol{I}$, where the constant $M_0 = \mathrm{Tr}(\boldsymbol{M}_0)/2$ is half the average over all boxes of the squared wall length. We implicitly assume that the volume is conserved, which should be correct in Couette flow. More precisely, to avoid overestimating M_0 owing to bubble stretching, we take the average between $\langle\ell\rangle^2/2$ and $\langle\ell^2\rangle/2$; since here $\langle\ell\rangle = 1.40\,\mathrm{mm}$ and $\sqrt{\langle\ell^2\rangle} = 1.45\,\mathrm{mm}$, we take $M_0 = 1.0\,\mathrm{mm}^2$.

3.3.3. *Elastic strain tensor*

We can operationally measure the *statistical elastic strain tensor* $\boldsymbol{U}$ in each box from (Aubouy *et al.* 2003):

$$\boldsymbol{U}(\boldsymbol{r}) = \frac{\log \boldsymbol{M}(\boldsymbol{r}) - \log \boldsymbol{M}_0}{2}. \tag{3.12}$$

It obeys (Aubouy *et al.* 2003) the mathematical requirements for a strain tensor: symmetry properties under translation, rotation and index permutation. It is always defined: $\log \boldsymbol{M}$ is the tensor with the same eigenvectors as $\boldsymbol{M}$, but with the logarithm of its (strictly positive) eigenvalues. It is the only dimensionless function of $\boldsymbol{M}$ and $\boldsymbol{M}_0$ which is always defined (there is no equivalent of the division for tensors, except when they commute).

It also obeys the physical requirements for an elastic strain tensor. It statistically quantifies the deformation reversibly stored in the present state of the material. Its differential $\mathrm{d}\boldsymbol{U}$ (and hence the elastic moduli for infinitesimal deformation around the current state) depends explicitly only on the current state.

Moreover, let us consider the case where the (small or large) deformation is elastic and affine. Then:

$$\left.\begin{aligned} \boldsymbol{\ell} &= \boldsymbol{F}\,\boldsymbol{\ell}_0, \\ \boldsymbol{\ell}\otimes\boldsymbol{\ell} &= \boldsymbol{\ell}\,\boldsymbol{\ell}^t = \boldsymbol{F}\boldsymbol{\ell}_0\boldsymbol{\ell}_0^t\,\boldsymbol{F}^t = \boldsymbol{F}(\boldsymbol{\ell}_0\otimes\boldsymbol{\ell}_0)\boldsymbol{F}^t, \\ \boldsymbol{M} &= \langle\boldsymbol{\ell}\otimes\boldsymbol{\ell}\rangle = \boldsymbol{F}\langle\boldsymbol{\ell}_0\otimes\boldsymbol{\ell}_0\rangle\boldsymbol{F}^t = \boldsymbol{F}\boldsymbol{M}_0\boldsymbol{F}^t. \end{aligned}\right\} \tag{3.13}$$

If we now assume that $\boldsymbol{M}_0$ commutes with $\boldsymbol{F}$, which is the case if for instance $\boldsymbol{M}_0$ is isotropic, then $\boldsymbol{M} = \boldsymbol{M}_0\boldsymbol{F}\boldsymbol{F}^t$. We then prove that $\boldsymbol{U}$ coincides with the true strain (Hoger 1987; Zimmerman 1999):

$$\boldsymbol{U} = \frac{\log \boldsymbol{M} - \log \boldsymbol{M}_0}{2} = \frac{\log(\boldsymbol{M}_0\boldsymbol{F}\boldsymbol{F}^t) - \log \boldsymbol{M}_0}{2} = \tfrac{1}{2}\log(\boldsymbol{F}\boldsymbol{F}^t) = \boldsymbol{E}^{(0)}, \tag{3.14}$$

see (3.8) and (3.10). The left Cauchy–Green tensor appears because we base our elastic description on a tensor, $\boldsymbol{\ell}\otimes\boldsymbol{\ell} = \boldsymbol{\ell}\,\boldsymbol{\ell}^t$. This constrasts with classical elasticity, based on a scalar product $\mathrm{d}\boldsymbol{x}\cdot\mathrm{d}\boldsymbol{x} = \mathrm{d}\boldsymbol{x}^t\mathrm{d}\boldsymbol{x} = \mathrm{d}\boldsymbol{x}_0^t\boldsymbol{F}^t\boldsymbol{F}\,\mathrm{d}\boldsymbol{x}_0$, where the right Cauchy–Green tensor appears (Phan-Thien 2002).

A specific feature of the quasi-static regime is that the deformation (and hence the elastic strain) remains small, barely visible by eye (figure 1), even for large applied

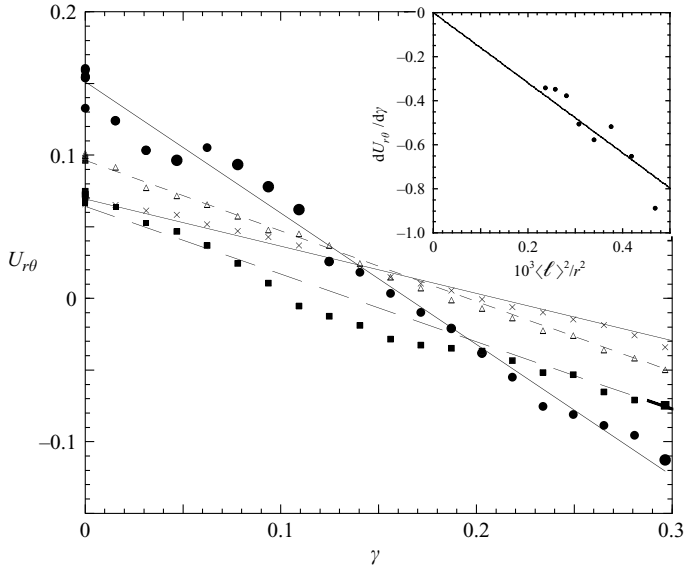

FIGURE 4. Run 1 (transient regime): cross-component $U_{r\theta}$ versus the applied shear strain γ, for ●, box 1; ■, box 3; △, box 5 and ×, box 7. Since $\gamma = 0$ marks the reversal of the rotation (and not an initially unstrained state), we expect $U_{r\theta}$ to be zero when $\gamma = 0.15$, within experimental error (± 0.03). A linear fit of $U_{r\theta}$ versus γ yields the derivative $dU_{r\theta}/d\gamma$, plotted in the inset, where the line is a linear fit with zero intercept to $dU_{r\theta}/d\gamma$ versus $1/r^2$.

shear strain (and hence large plastic strain). We thus assume, and check *a posteriori* (figure 7), that the components of $\boldsymbol{U}$ are much smaller than 1, so we approximate (3.12) by its linearization:

$$\boldsymbol{U}(\boldsymbol{r}) \approx \tfrac{1}{2}\left(\frac{\boldsymbol{M}(\boldsymbol{r})}{M_0} - \boldsymbol{I}\right). \tag{3.15}$$

4. Results

4.1. *Transient regime*

All data in this section are taken from Run 1 (figure 1), which has two distinct regimes: a transient and a stationary flow (figure 3).

4.1.1. *Texture tensor*

In the *transient regime*, the average wall length does not change much, but the walls tend to align with the direction of the rotation (figure 1). Hence, it is mostly the cross-component $M_{r\theta}$ which correlates to the shear (figure 3). Since $\gamma = 0$ marks the change from clockwise to counterclockwise shear, $M_{r\theta}$ decreases linearly and changes sign. The correlation with shear of both other components, if any, is of order of their fluctuations.

4.1.2. *Elastic strain tensor*

During the transient, no bubble rearrangement (neighbour swapping, also called 'T1 processes') is visible for $\gamma < 0.3$. This probably corresponds to the elastic regime (Höhler, Cohen-Addad & Hoballah 1997). The cross-component $U_{r\theta}$ varies linearly with γ, and a linear fit yields its derivative $dU_{r\theta}/d\gamma$ (figure 4). It varies smoothly with r, and a fit to r^{-2} yields the prefactor $(-1600 \pm 90)\langle\ell\rangle^2$.

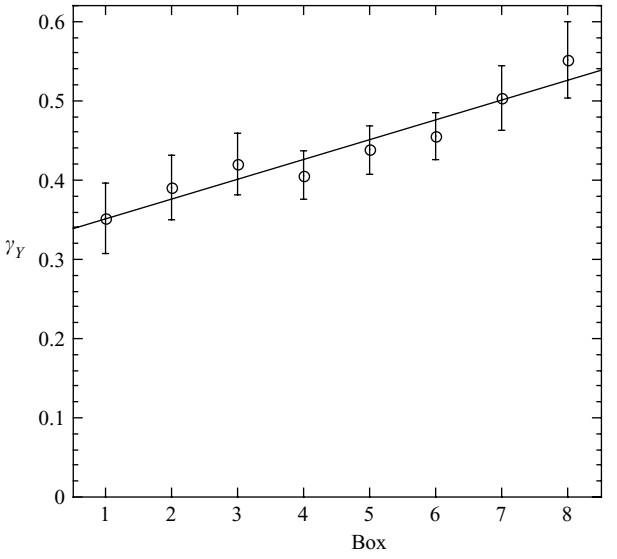

FIGURE 5. Run 1 (transient regime): variation of γ_Y versus box number. Data are from figure 3. The line is a linear fit.

It is interesting to compare $\mathrm{d}U_{r\theta}/\mathrm{d}\gamma$ with the expression which would be predicted by classical elasticity in a Couette geometry:

$$\frac{\mathrm{d}U_{r\theta}}{\mathrm{d}\gamma} = \frac{r_1^2 r_0}{r_1 + r_0}\,\frac{1}{r^2}. \tag{4.1}$$

The prefactor of (4.1) is $(r_1^2 r_0)/[(r_1 + r_0)] = (-1680 \pm 80)\langle \ell \rangle^2$, where we have taken 1.2 mm (the depth of the teeth) as the uncertainty of the wheel radius. This agrees with the experimental prefactor of r^{-2} (figure 4).

4.1.3. *Yield*

The flow becomes stationary at a value γ_Y which we measure by determining the intersection between the transient buildup of $M_{r\theta}$ fitted by a straight line and the stationary plateau fitted by a horizontal line (figure 3). It would be interesting to determine whether γ_Y actually marks the onset of irreversibility in the stress–strain relation at macroscopic scale (plasticity).

We can at least observe on the movie (data not shown) the 'T1' bubble rearrangements, which concern local topology. In the inner boxes, γ_Y correlates with the appearance of a large number of T1s. The first isolated T1s appear at values of γ between 0.26 and 0.32, of the same order of magnitude as, but significantly smaller than γ_Y. The outer boxes lack T1s, except once near $\gamma \sim 3$, well beyond γ_Y and in the stationary regime. Though γ_Y is well defined, it marks a saturation in the local shear strain applied to the bubbles, which probably oscillates and remains below the actual yield strain.

The value of γ_Y increases gradually from 0.35 for the inner box, to 0.55 for the outer box (figure 3). Within experimental error (± 0.03, corresponding to ± 2 images), this variation is linear (figure 5). Explaining this variation of γ_Y with r would certainly help us to understand the yielding of foams (see § 5.2.2).

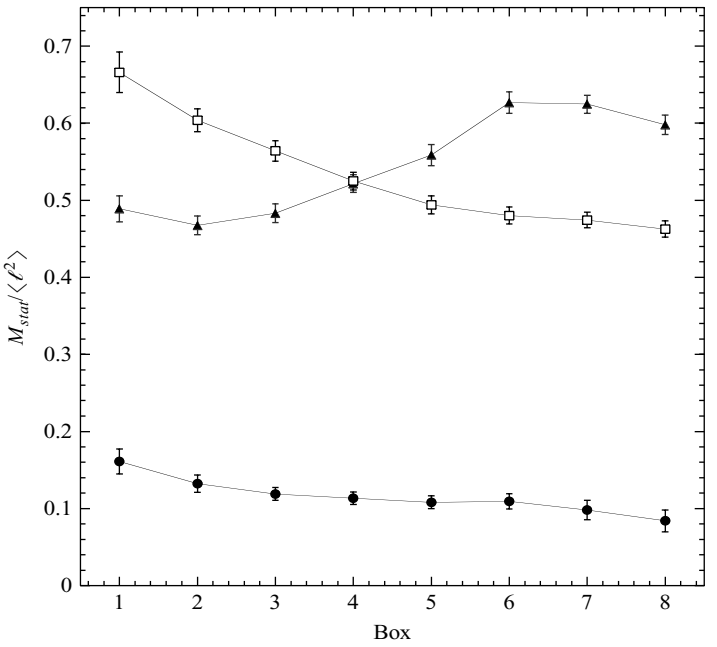

FIGURE 6. Run 2 (stationary flow): texture tensor $\boldsymbol{M}_{stat}$ versus box number. The components of $\boldsymbol{M}$ (▲, M_{rr}; □, $M_{\theta\theta}$; ●, $M_{r\theta}$), again expressed in units of $\langle \ell^2 \rangle$, are averaged over the four quarters of the whole foam, and also over time (2000 pictures).

4.2. *Stationary regime – average values*

All data of this section are taken from Run 2 (figure 2), which allows us to improve our statistics, using temporal averages over the stationary flow.

4.2.1. *Texture tensor*

Figure 6 plots the average M_{stat} of the instantaneous texture tensor $\boldsymbol{M}$ in the stationary regime. We can now detect, not only the (small) anisotropy of the foam, $M_{r\theta}$, but also its small spatial variations.

$M_{r\theta}$ decreases across the gap: it is larger in the inner boxes than in the outer ones, reflecting the preferred orientation imposed by the shear. M_{rr} decreases, $M_{\theta\theta}$ increases, and $M_{rr} - M_{\theta\theta}$ changes sign; this sign-change is more difficult to understand (§ 5.1.3).

4.2.2. *Elastic strain*

$U_{r\theta}$ does not localize near the inner wheel; it varies smoothly with the distance to the inner wheel. It decreases as $\sim 1/r^2$ (figure 7), as expected if the foam behaves like a continuous elastic medium, see (4.1).

To compare to the transient regime in Run 1 (which has slightly different bubble and wheel diameters), we express the prefactor determined in figure (7) in the same units as in (4.1):

$$\langle U_{r\theta} \rangle = \gamma_{el} \frac{r_1^2 r_0}{r_1 + r_0} \frac{1}{r^2}. \tag{4.2}$$

The prefactor is $\gamma_{el} = 0.171 \pm 0.003$, see § 5.2.2.

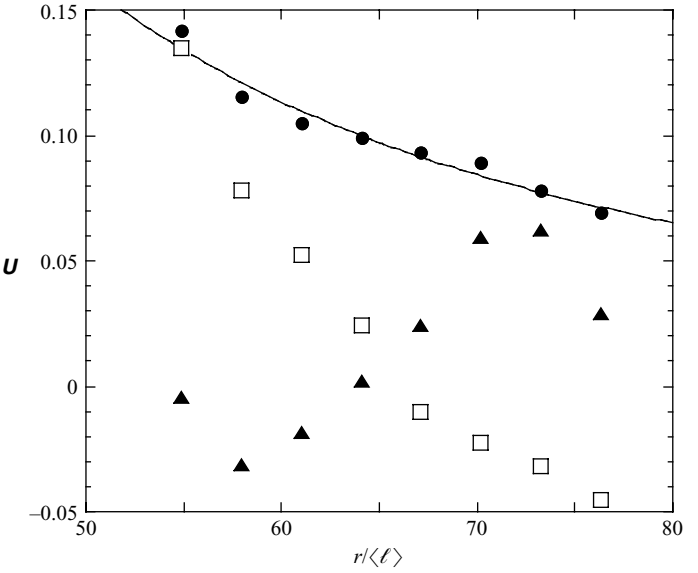

FIGURE 7. Run 2 (stationary flow): tensor $\boldsymbol{U}$ versus box number. The components of $\boldsymbol{U}$ (▲, U_{rr}; □, $U_{\theta\theta}$; ●, $U_{r\theta}$) are derived from the data in figure 6 through (3.15), using the value $M_0 = 1.0\,\mathrm{mm}^2$ (see § 3.3.2). The solid line is a best fit of $U_{r\theta}$ to a function cst/r^2.

4.2.3. *Deviatoric elastic stress*

In the quasi-static regime, mechanical equilibrium implies that the elastic stress is divergence free. Hence, we expect that its off-diagonal component, which reduces to the capillary contribution, varies as for a continuous elastic medium in a Couette geometry (Dennin 2004): $\sigma_{r\theta}^{cap} \sim \mathrm{cst}/r^2$. Such r^{-2} dependence occurs experimentally (figure 8).

Again, the spatial variation of $\sigma_{rr}^{cap} - \sigma_{\theta\theta}^{cap}$, which changes sign, is more difficult to understand (§ 5.1.3).

4.2.4. *Non-dimensional shear modulus*

In elasticity, the stress and the deformation are conceptually independent quantities (see § 5.1.2). In a continuous medium, they correlate physically; their relation is the elastic part of the material's constitutive relation (Landau & Lifschitz 1986). Let us focus on the components we measure here, namely the deviatoric terms $rr - \theta\theta$ and $r\theta$. If the material is linear, the components of strain and stress are proportional to each other, the slope being twice the shear modulus μ. If the material is isotropic, $rr - \theta\theta$ and $r\theta$ play a similar role. In polar coordinates, the Hooke equations becomes:

$$\sigma_{r\theta}^{cap} = 2\mu U_{r\theta}, \tag{4.3}$$

$$\left(\sigma_{rr}^{cap} - \sigma_{\theta\theta}^{cap}\right) = 2\mu(U_{rr} - U_{\theta\theta}). \tag{4.4}$$

Figure 9 indicates that, in the quasi-static regime, the foam indeed behaves like a continuous medium: the deviatoric part of the capillary stress $\boldsymbol{\sigma}^{cap}$ and of $\boldsymbol{U}$ correlate strongly, and details of the microstructure appear only through mesoscopic averages. Moreover, the foam is both isotropic and linear, with a shear modulus $\mu = (0.59 \pm 0.02)\lambda/\langle\ell\rangle$. With a smaller or a larger box size, we obtain the same value for μ with a larger uncertainty.

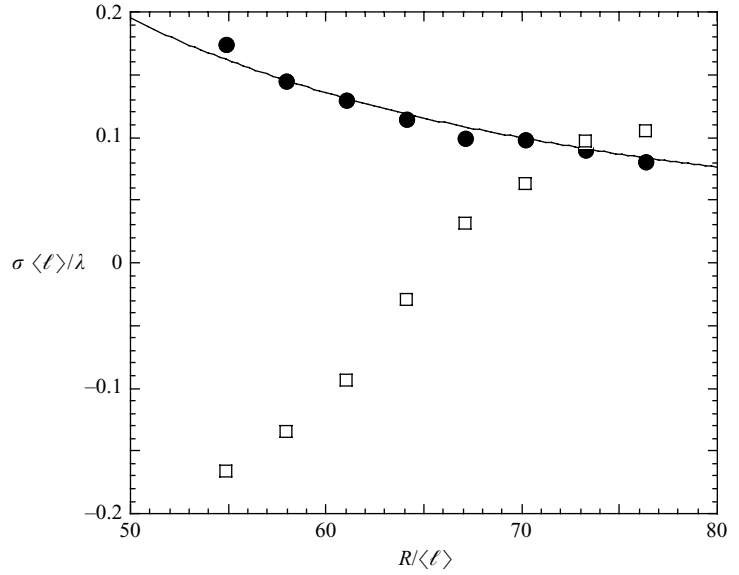

FIGURE 8. Run 2 (stationary flow): elastic stress tensor $\boldsymbol{\sigma}^{cap}$ versus box number. The deviatoric components of $\boldsymbol{\sigma}^{cap}$ (●, shear stress $\sigma_{r\theta}^{cap}$; □, normal stress difference $\sigma_{rr}^{cap} - \sigma_{\theta\theta}^{cap}$) are derived from (3.5) and expressed in units of $\lambda/\langle\ell\rangle$. The solid line is a best fit of $\sigma_{r\theta}^{cap}$ to a function cst/r^2.

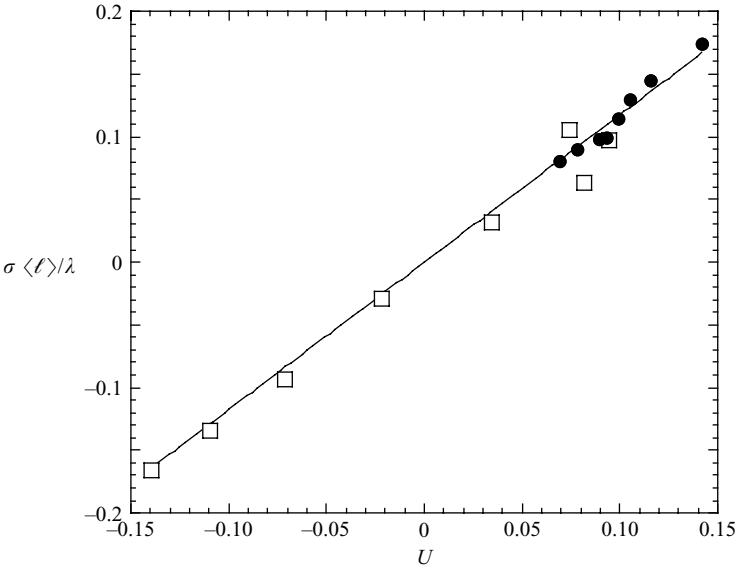

FIGURE 9. Run 2 (stationary flow): Hooke relation. The deviatoric part of the capillary stress $\boldsymbol{\sigma}^{cap}$, expressed in units of $\lambda/\langle\ell\rangle$, plotted versus the corresponding components of $\boldsymbol{U}$ (●, $\sigma_{r\theta}^{cap}$ versus $U_{r\theta}$; □, $\sigma_{rr}^{cap} - \sigma_{\theta\theta}^{cap}$ versus $U_{rr} - U_{\theta\theta}$). Each data point comes from figures 7 and 8, i.e. it derives from averages at one position in the foam. The solid line is a linear fit through all points, slope $2\mu\langle\ell\rangle/\lambda = 1.17 \pm 0.04$.

4.3. *Permanent regime – temporal fluctuations*

4.3.1. *Time series of* $\boldsymbol{M}$ *in Run 1*

The stationary flow results from a balance between the increase due to the applied shear strain and relaxation due to bubble rearrangements (Langer & Liu 1997). The texture tensor and the elastic strain fluctuate around their mean value.

In Run 1, the short-term fluctuations are much larger near the inner wheel (figure 3*a*), where shape deformations and bubble rearrangements are both larger (Debrégeas *et al.* 2001), than near the outer wheel (figure 3*b*). Figure 3 does not show any significant physical feature of the fluctuation statistics, e.g. abrupt large-scale relaxations of deformations *via* correlated, large stress drops.

4.3.2. *Histograms of increments in Run 2*

We perform a more quantitative analysis on Run 2, at a small scale, namely between two successive images, corresponding to an increase of $\mathrm{d}\gamma$ in the applied shear strain. The increment of the texture tensor is defined as $\boldsymbol{M}(\gamma + \mathrm{d}\gamma) - \boldsymbol{M}(\gamma)$. The signature of 'avalanche-like' events at such a small scale would be extremely large fluctuations and/or a large asymmetry between positive and negative increments.

We find no such signature. The increments are almost Gaussian (figure 10*a–c*). The width of the histograms decreases by a factor of 10 from inner to outer boxes (figure 10*d*); as we mentioned, most large fluctuations occur near the inner wheel. Only $M_{r\theta}$ displays a slight asymmetry between positive and negative increments (figure 10*b*), probably because this cross-component is increased by the applied shear strain and decreased by the anisotropy relaxation due to T1 events.

4.3.3. *Temporal autocorrelations in Run 2*

The rotation of the inner wheel does not perturb the foam near the outer wheel. In the outer boxes, the texture tensor thus decorrelates very slowly. Let us quantify this observation using the data of Run 2.

To analyse the fluctuations at all scales of the shear strain $\delta\gamma$, we calculate the temporal autocorrelation C_{MM} of the fluctuations:

$$C_{MM}(\delta\gamma) = \frac{\langle (M(\gamma) - M_{\mathrm{stat}})(M(\gamma + \delta\gamma) - M_{\mathrm{stat}})\rangle}{\langle (M(\gamma) - M_{\mathrm{stat}})^2\rangle}, \tag{4.5}$$

where $M(\gamma)$ (resp: M_{stat}) is the instantaneous value (resp: the average over the stationary regime) of the texture tensor $\boldsymbol{M}$.

Figure 11 displays a rapid initial decay in the correlation, followed by a slower decay, reflecting the destruction of the initial conditions (Durian 1997; Lauridsen, Twardos & Dennin 2002; Ybert & di Meglio 2002; Pratt & Dennin 2003). An exponential fit at small $\delta\gamma$ yields the shear strain γ_{decorr} characterizing the initial loss of correlation, especially quick for the cross-component $M_{r\theta}$ (figure 12):

$$C_{M_{r\theta}M_{r\theta}} = \exp\left(-\frac{\delta\gamma}{\gamma_{decorr}}\right). \tag{4.6}$$

As we expect, the correlation decays much more quickly near the inner wheel, $\gamma_{decorr} \approx 1/30$, than near the outer one, $\gamma_{decorr} \approx 1$ (insert of figure 12). The decorrelation rate γ_{decorr}^{-1} decreases exponentially with the distance from the inner wheel.

The fluctuations of the texture tensor are thus localized near the inner wheel, over a distance comparable to four bubble diameters. This localization resembles that of

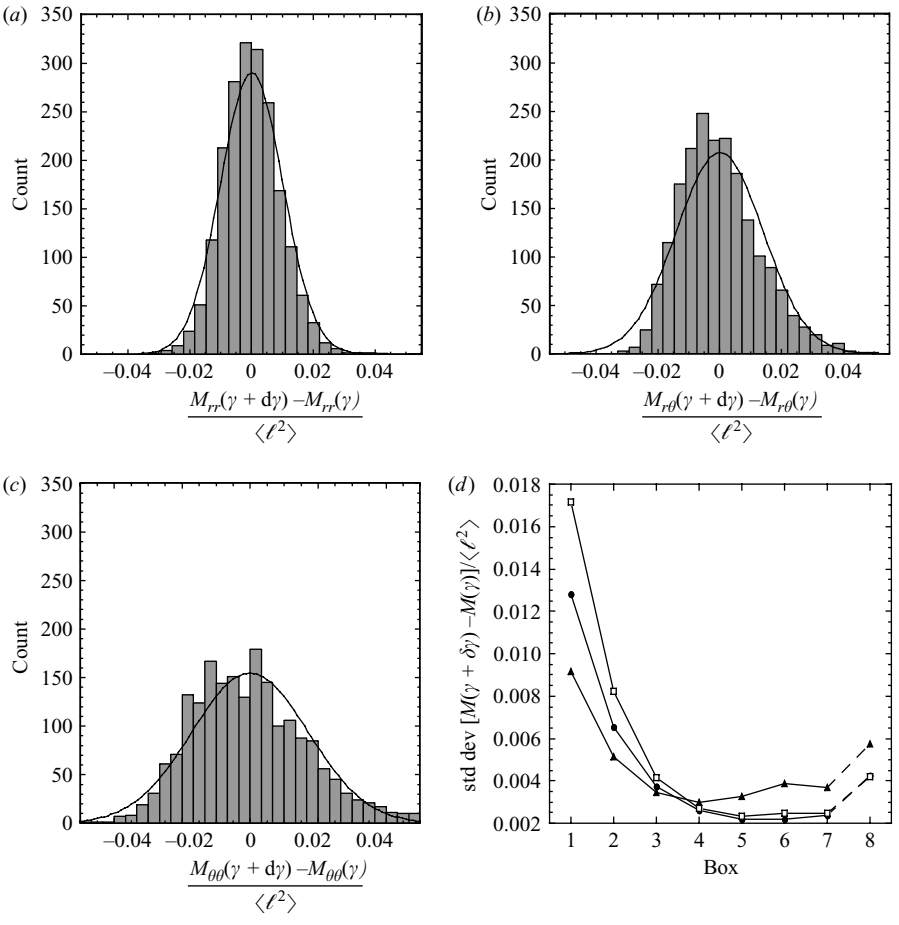

FIGURE 10. Run 2 (stationary flow): statistics for the increments of the texture tensor $\boldsymbol{M}$. (*a*) Histogram of increments of M_{rr} in box 1, again expressed in units of $\langle \ell^2 \rangle$. Solid line is a Gaussian with the same standard deviation and zero average. (*b*, *c*) The same for $M_{r\theta}$ and $M_{\theta\theta}$. (*d*) Standard deviation of increments of $\boldsymbol{M}$ versus box number (▲, M_{rr}; □, $M_{\theta\theta}$; ●, $M_{r\theta}$). Since the fluctuations in box 8 are extremely small (see figure 3), the data are noisy: image filtering and thresholding would have been required to obtain a statistically significant value.

the velocity field over one bubble diameter (Debrégeas *et al.* 2001), and is probably the signature of the effect of T1s on the deformation (Dennin 2004).

5. Discussion

5.1. *Discussion of the strain and stress*

5.1.1. *Measurement method of the stress*

Let us discuss the contributions to the stress we do not measure.

The dissipation is probably dominated by the friction on both glass plates, which we expect to be much larger than the internal viscous stress (Cantat, Kern & Delannay 2004). Whatever its physical origin, it should on average balance the input power. It is thus never negligible, especially during the relaxation after each T1, see § 2.1.

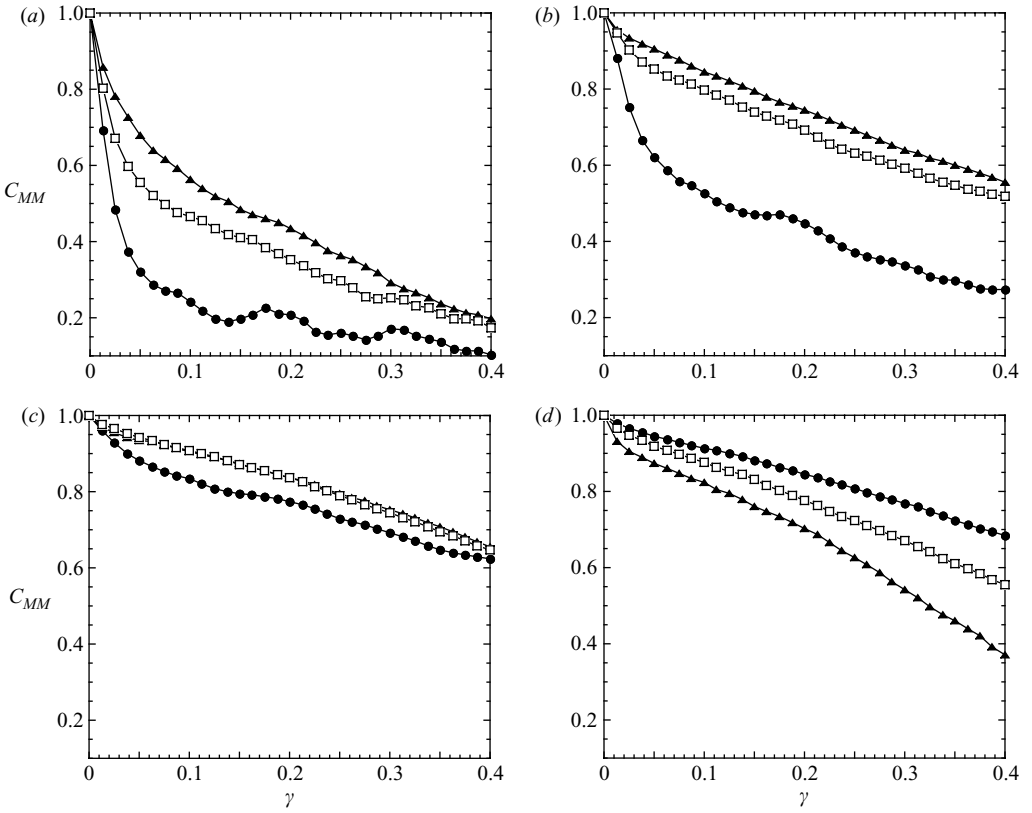

FIGURE 11. Run 2 (stationary flow): temporal autocorrelation C_{MM} of texture tensor $\boldsymbol{M}$ (equation (4.5)), versus $\delta\gamma$, in boxes (*a*) 1, (*b*) 3, (*c*) 5, (*d*) 7 (▲, M_{rr}; □, $M_{\theta\theta}$; ●, $M_{r\theta}$). We recall that the total applied shear γ is proportional to time, not to the local shear in each box, (2.1).

However, the results we present here, which concern only the elastic terms, do not require us to measure the dissipation.

We measure the deviatoric elastic stress using (3.5), which is formally equivalent to the stress in a network where sites interact through a two-body force. Foams do not include only two-vertex interactions. Their stability is due to the pressure inside each bubble, which relates to the bubble volume. Hence, pressure is a function of all wall curvatures and all the vertex positions. It is an n-body interaction, which we can decompose into two-point interactions in principle (Alexander 1998), but not really in practice.

It is not important here to measure the pressure inside bubbles, for the following reasons (Graner 2002). Since the pressure stress is isotropic, it does not contribute to the deviatoric elastic stress. Hence, the shear modulus is independent of the pressure field. Finally, the compression modulus of a foam is typically that of an ideal gas, which scales like the pressure inside bubbles $\sim 10^5$ Pa (multiplied by h, when expressed as a two-dimensional compression modulus). This modulus is not relevant here and is much larger than the shear modulus of the foam, which is thus effectively incompressible (Weaire & Hutzler 1999).

The line tension is not known, but is unimportant for our present purposes. The stress, and hence the shear modulus, are expressed in non-dimensional form, as required for comparison to other foams. A direct measurement of λ can complement

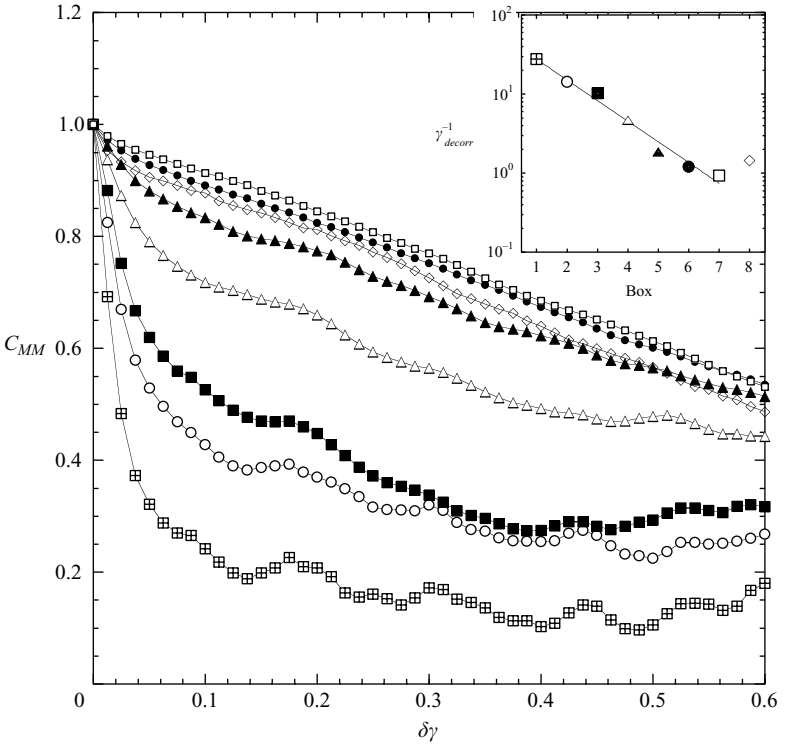

FIGURE 12. Run 2 (stationary flow): autocorrelation $C_{M_{r\theta}M_{r\theta}}$ of the cross-component $M_{r\theta}$. ⊞, box 1; ○, box 2; ■, box 3; △, box 4; ▲, box 5; ●, box 6; □, box 7; ◇, box 8. Inset: initial decorrelation rate γ^{-1}_{decorr} for each box, (4.6).

the local image measurement when necessary, for instance to predict the actual force exerted by the flowing foam on an obstacle, or to validate (3.5) by checking its agreement with an independent, macroscopic measurement of the force (Courty *et al.* 2003).

5.1.2. *Difference between* $\boldsymbol{\sigma}^{cap}$ *and* $\boldsymbol{M}$

Both $\boldsymbol{\sigma}^{cap}$ and $\boldsymbol{M}$ are measured from the same image, and their definitions ((3.5) and (3.11)) appear similar. However, they are really independent, both physically and mathematically.

Physically, their significance and status are different. The value of $\boldsymbol{\sigma}^{cap}$ can be determined from image analysis only if the sites interact through a two-body force $\boldsymbol{\tau}$, and if we explicitly know the form of this force $\boldsymbol{\tau}(\boldsymbol{\ell})$ with respect to the distance between sites. The value of $\boldsymbol{\sigma}^{cap}$ is sensitive to physical forces: first, it doubles if the density of links doubles; secondly, it does not change if we cut a link in two by artificially introducing a new site at its middle; thirdly, in foams, it formally depends on wall curvatures.

On the other hand, $\boldsymbol{M}$ is purely geometric. It is a characteristic of the pattern, independent of physical interactions; it can be defined and measured for various kinds of cellular patterns for which no $\boldsymbol{\tau}$ can be defined, including solid foams, and even grain boundaries in crystals (Durand, Weiss & Graner 2004). The value of $\boldsymbol{M}$ is sensitive to the detailed network topology: first, it does not change if the density of walls doubles; secondly, it decreases if we cut a wall in two by artificially introducing

a new vertex at its middle; thirdly, in foams, it is insensitive to the (in-plane or out-of-plane) curvature of walls.

Mathematically, $\boldsymbol{\sigma}^{cap}$ and $\boldsymbol{M}$ are independent in all cases, except when $\boldsymbol{\tau} \propto \boldsymbol{\ell}$, i.e. a harmonic spring, with a length ℓ much greater than its length at equilibrium. For instance, writing the stress of an isolated polymer molecule in a shear solvant as $\boldsymbol{\ell} \otimes \boldsymbol{\ell}$ is legitimate (Bird, Armstrong & Hassager 1987). However, foams, for which $\tau = \text{const}$, fall in the general case where $\boldsymbol{\sigma}^{cap}$ and $\boldsymbol{M}$ are mathematically different averages. The difference is even more visible in a three-dimensional foam, where $\boldsymbol{\sigma}^{cap}$ is an integral over a surface (Batchelor 1970), while $\boldsymbol{M}$ remains based on vectors (Aubouy *et al.* 2003).

Moreover, $\boldsymbol{M}$ does not even need be defined on the vectors $\boldsymbol{\ell}$ linking neighbour vertices (whereas $\boldsymbol{\sigma}^{cap}$ must be). Definitions other than (3.11) could be acceptable in principle (B. Dollet, personal communication). For instance, we could use the vector $\boldsymbol{g}$ which links the centres of mass of neighbouring bubbles, and construct $\boldsymbol{M}$ as $\langle f\, \boldsymbol{g} \otimes \boldsymbol{g} \rangle$. This would apply to bubble rafts (Dennin 2004), granular materials (Kruyt 2003), or three-dimensional foams (Kraynik, Reinelt & van Swol 2003). This would change both $\boldsymbol{M}$ and $\boldsymbol{M}_0$ by a multiplicative constant: the elastic strain $\boldsymbol{U}$ ((3.12) and (3.15)), and hence the shear modulus μ, (4.4), would almost not change.

We emphasize that $\boldsymbol{\sigma}^{cap}$ and $\boldsymbol{U}$ are also independent. They represent different averages of microscopic details, so we cannot express one as a function of the other (Goldhirsch & Goldenberg 2002; Kruyt 2003), except empirically, through numerical simulations or physical approximations (Kruyt 2003). The difference is even more visible at large deformations: the logarithmic term of (3.12) deviates from the linear approximation when the maximum value of the elastic shear strain (0.15 in figure 7) reaches large values, e.g. 0.4 (Courty *et al.* 2003) or 0.6 (Asipauskas *et al.* 2003). There is no trivial relation between them, except in a regular pattern, where averages are replaced by exact identities; for instance, in the case of a honeycomb, their relation is exactly as expected (B. Dollet, personal communication).

5.1.3. *Sign of normal differences*

The normal differences $M_{rr} - M_{\theta\theta}$ and $\sigma_{rr}^{cap} - \sigma_{\theta\theta}^{cap}$ change sign in the middle of the gap, between boxes 4 and 5 (figures 6, 7 and 8).

Normal stresses appear in elastic solid (Poynting 1909) or granular (Bagnold 1941) materials sheared at constant volume (this is equivalent to 'dilatancy': volume increase under shear at constant pressure Weaire & Hutzler 2003). In complex fluids such as foams, these normal stresses exist, but are difficult to measure (Khan, Schnepper & Armstrong 1988) and to predict (Weaire & Hutzler 2003). Predictions and two-dimensional simulations of their average are accurate: under steady shear, the pressure of a foam with fluid fraction $\Phi = 5\,\%$ increases by 15 % (Weaire & Hutzler 2003). This is the order of magnitude of the spatial variations of M_{rr} and $M_{\theta\theta}$ (figure 6). We cannot predict their anisotropy (hence the normal stress differences), but normal stresses due to dilatancy are a second-order effect in the strain (Larson 1997): they are probably smaller than the large value of $M_{rr} - M_{\theta\theta}$ we observe, and might be masked by dynamical effects due to bubble rearrangements. However, we can imagine other explanations.

First, this change could reflect an initial anisotropy resulting from the procedure used to fill the cell with foam (Debrégeas *et al.* 2001), which the preparatory rotation does not suffice to relax in the outer boxes (G. Debrégeas, personal communication). The initial state is not necessarily a zero-stress state. More generally, trapped stresses make notoriously difficult to measure normal stress differences (Khan, Schnepper &

Armstrong 1988), and carefully relaxed simulations are more reliable (Kraynik *et al.* 2003). The present measurement is probably one of the first direct experimental ones, along with that of Labiausse, Höhler & Cohen-Addad (2005).

Secondly, it could be an artefact owing to our measurement method, which does not account for the out-of-plane curvature of bubble walls (in the third dimension). Since the foam is not perfectly dry, the sides of the walls can have slightly different curvatures, so that their contributions would not exactly cancel out.

Thirdly, this change could arise from a deviation from axisymmetric Couette flow, owing to a secondary recirculation with radial velocity components. A signature of the discrete and disordered nature of the material is the appearance of solid-body rotation of bubble clusters. It results in vortices, generic for amorphous elastic materials, generated by the 'backflow' of the non-affine displacements (Tanguy *et al.* 2002). Their lifetime is as short as the time the internal wheel takes to move one bubble diameter (Debrégeas *et al.* 2001).

5.2. *Discussion of the stationary flow*

The present measurements clarify a few open debates.

5.2.1. *To localize or not to localize?*

The experimental set-up, the fluid fraction, the friction on the plates, and the boundary conditions at the wheel, are those of Debrégeas *et al.* (2001). How can the same data alternatively display and not display localization?

There is no fundamental incompatibility: different fields have different spatial variations. Debrégeas *et al.* (2001) measure the velocity field, and the T1 rate; while we measure the elastic stress and strain fields. In a quasi-static regime, where the foam is almost always close to mechanical equilibrium, we expect the stress to vary smoothly across the gap, as observed here and in simulations (Kabla & Debrégeas 2003). The elastic strain, which correlates to the elastic stress, does not localize, although the plastic strain, which correlates to the velocity gradient, does.

5.2.2. *Yield*

The value of the yield strain and stress, characterized, for example, by the equality of the real and imaginary parts of the complex shear modulus (Höhler, Cohen-Addad & Asnacios 1999), is not completely understood yet. It generally depends on the shear rate (Coussot *et al.* 2002; Rouyer *et al.* 2003), but not in the present quasi-static regime.

We expect that, to store a deformation γ_{el}, requires us to apply an equivalent shear strain γ_Y. Since Run 1 corresponds to an inversion from counterclockwise to clockwise rotation, we expect that $\gamma_Y = 2\gamma_{el}$. We observe an excellent agreement in box 1, in which $\gamma_Y = 0.35 \pm 0.02$ (figure 3) and $\gamma_{el} = 0.171 \pm 0.003$ (figure (7) and (4.2)). However, $\gamma_Y \neq 2\gamma_{el}$ in other boxes, for larger γ_Y (figure 5). Thus the deformation stored in the foam changes with γ even above γ_Y. Kabla & Debrégeas (2003) reach the same conclusion: their simulations indicate that, after the foam yields, T1s localize in the shear band only after a certain delay time.

5.2.3. *Averages and fluctuations*

Our data show that stress and strain have a well-defined physically meaningful average at the scale of a representative volume element, while their fluctuations remain small. A coarse-grained shear modulus can be defined and measured, unlike, for example, in granular media, where the importance of fluctuations at large scales is still an open debate (Goldenberg & Goldhirsch 2004).

More precisely, the statistics of the texture tensor are nearly Gaussian. Visual inspection of the images confirms that T1s remain isolated. They correlate (Kabla & Debrégeas 2003), but over a very small space and time range, probably owing to the experimental conditions: disordered foam, quasi-static regime, large dissipation due to top and bottom plates. We do not observe extremely large fluctuations, nor sudden relaxations of deformations and stress.

Averages seem to dominate the physics (figure 3), but fluctuations too are important. For instance, the width of the histogram of the velocity or stress field fluctuations might constrain the velocity field, and explain why shear-banding occurs preferentially near the inner wheel, owing to a feedback loop on which fluctuations grow (Kabla & Debrégeas 2003).

Both the average and fluctuations of the T1 rate manifest themselves in the texture tensor. The signature of the average T1 rate is the existence of a stationary regime, where the decrease in deformation due to T1s balances the increase due to applied shear. The signature of T1 rate fluctuations is the exponential localization of the texture tensor fluctuations.

5.2.4. *Measurement of the shear modulus*

Figure 9 leads to a few remarks. First, the classical method of measuring a shear modulus consists in increasingly deforming a sample, and measuring the stress and strain in successive states. We use here another method (Asipauskas *et al.* 2003). Each point in figure 9 comes from a different region of the same foam. We thus observe different deformation states simultaneously from a single heterogeneous image. Averaging over successive images reduces noise (Asipauskas *et al.* 2003), but is not necessary (Courty *et al.* 2003; Durand *et al.* 2004).

Secondly, when determining the constitutive relation for plastic materials, the elastic stress is classically plotted *versus* the total applied shear strain (see e.g. Jiang *et al.* 1999; Reinelt & Kraynik 2000; Weaire & Hutzler 2003). Different applied strains correspond to the same stress. Here we observe a one-to-one correspondence between elastic stress and elastic strain (figure 9). The foam is elastic, although the plastic strain increases steadily, and the foam is well beyond the yield strain.

Thirdly, although we do not know the value of λ, we can compare our non-dimensional measurement of shear modulus μ with published values. An ideal two-dimensional dry monodisperse foam, where bubbles form a regular honeycomb lattice (Princen 1983; Khan & Armstrong 1986; Weaire & Hutzler 1999), has a shear modulus $\mu_{hc} = \lambda/\sqrt{3}\langle\ell\rangle = 0.577\lambda/\langle\ell\rangle$. Our μ is slightly larger, probably owing to disorder; here $\langle\ell^2\rangle/\langle\ell\rangle^2 = 1.08$. The non-zero fluid fraction tends to decrease μ (Princen 1983; Khan & Armstrong 1986; Mason, Bibette & Weitz 1995; Weaire & Hutzler 2003). In a non-quasi-static, and more heterogeneous, stationary flow, either through a constriction or around an obstacle, a dry foam (fluid fraction much lower than 5 %), even with a small bubble size dispersity < 5 %, displays a shear modulus 20 % higher than μ_{hc}, owing to the stretched bubble shape ($\langle\ell^2\rangle/\langle\ell\rangle^2 = 1.22$ Asipauskas *et al.* 2003).

6. Conclusion

To summarize, we re-analyse the data generously provided by G. Debrégeas on a foam sheared in a two-dimensional Couette geometry, with the velocity field localized near the inner wheel (Debrégeas *et al.* 2001). Since the flow is quasi-static, the deformation of the bubbles is very small. We take advantage of the foam's invariance under rotation (and, in the stationary regime, of its time invariance) to average

over many bubbles. We then measure the texture tensor of the foam, a general tool to quantify the deformation of two-dimensional or three-dimensional networks and cellular patterns (Aubouy *et al.* 2003).

For small applied shear strain, a transient regime has the cross-component of the texture tensor increase linearly with shear, with no bubble rearrangements ('T1'), and the foam seems to behave like a classical elastic continuous medium. The only large-scale manifestation of the discrete cellular nature of the foam is that, in a mixture of two fluids (soap solution and air), the surface tension of bubble walls produces elastic behaviour and a shear modulus.

The deformation saturates first near the inner wheel, then gradually in more distant boxes, at an applied shear strain γ_Y. This onset of plastic behaviour correlates, but does not strictly coincide with the appearance of T1s.

The foam then enters a stationary regime, where the deformation increase due to shear and the relaxation due to T1s balance each other. The fluctuations of the texture tensor around its mean value remain small. Despite the T1s, the elastic behaviour of the foam again resembles that of a classical elastic continuous medium. The maximum shear strain that the foam can sustain in the quasi-static regime is γ_{el}, compatible with the value of γ_Y. The strain and stress are highly correlated, even proportional to each other; the shear modulus is slightly higher than for a honeycomb with similar average bubble wall length. The deviatoric components of the elastic strain and stress tensors, as well as the texture tensor, do not localize. The only trace of localization is the much quicker loss of correlation of the texture tensor fluctuations near the inner wheel.

Future studies aim at understanding the origin of the value of the yield strain, the change of sign in the normal stress and strain differences, the precise role of boundary conditions, and the relation to granular materials. They include the measures of pressure and dissipation, and the analytical calculation of the shear modulus.

We are extremely grateful to G. Debrégeas for providing us with many recordings of his published and unpublished experiments, and for detailed discussions. We would also like to thank M. Dennin, R. Höhler, A. Kabla, A. Kraynik, N. Kruyt, J. Scheibert for discussions, M. Aubouy, B. Dollet, F. Elias and J. A. Glazier for critical reading of the manuscript, and O. Cardoso for help with image analysis. This work was partially supported by CNRS ATIP 0693.

REFERENCES

Alexander, S. 1998 *Phys. Rep.* **296**, 65.

Asipauskas, M., Aubouy, M., Jiang, Y., Graner, F. & Glazier, J. A. 2003 *Granular Matt.* **5**, 71.

Aubouy, M., Jiang, Y., Glazier, J. A. & Graner, F. 2003 *Granular Matt.* **5**, 67.

Bagnold, R. A. 1941 *The Physics of Blown Sand and Desert Dunes.* Methuen.

Ball, R. & Blumenfeld, R. 2002 *Phys. Rev. Lett.* **88**, 115505.

Batchelor, G. K. 1970 *J. Fluid Mech.* **41**, 545.

Bird, R. B., Armstrong, R. C. & Hassager, O. 1987 *Dynamics of Polymeric Liquids.* John Wiley.

Blumenfeld, R. 2004 *Physica* A **336**, 361.

Cantat, I., Kern, N. & Delannay, R. 2004 *Europhys. Lett.* **65**, 726.

Courty, S., Dollet, B., Elias, F., Heinig, P. & Graner, F. 2003 *Europhys. Lett.* **64**, 709.

Coussot, P., Raynaud, J.-S., Bertrand, F., Moucheront, P., Guilbaud, J.-P., Huynh, H. T., Jarny, S. & Lesueur, D. 2002 *Phys. Rev. Lett.* **88**, 218301.

Cox, S. J., Weaire, D. & Vaz, M. F. 2002 *Eur. Phys. J.* E **7**, 311.

Debrégeas, G., Tabuteau, H. & Di Meglio, J.-M. 2001 *Phys. Rev. Lett.* **87**, 178305.

Dennin, M. 2004 *Phys. Rev.* E **70**, 041406.

Durand, G., Weiss, J. & Graner, F. 2004 *Europhys. Lett.* **67**, 1038.
Durian, D. J. 1997 *Phys. Rev.* E **55**, 1739.
Elias, F., Flament, C., Glazier, J. A., Graner, F. & Jiang, Y. 1999 *Phil. Mag.* B **79**, 729.
Farahani, K. & Naghdabadi, R. 2000 *Intl J. Solids Struct.* **37**, 5247.
Géminard, J.-C., Żywociński, A., Caillier, F. & Oswald, P. 2004 *Phil. Mag. Lett.* **84**, 199.
Goldenberg, C. & Goldhirsch, I. 2004 *Granular Matt.* **6**, 87.
Goldhirsch, I. & Goldenberg, C. 2002 *Eur. Phys. J.* E **9**, 245.
Graner, F. 2002 Two-dimensional fluid foams at equilibrium. In *Morphology of Condensed Matter – Physics and Geometry of Spatially Complex Systems* (ed. K. Mecke & D. Stoyan), p. 187–214. Lecture Notes in Physics. Springer.
Graner, F., Jiang, Y., Janiaud, E. & Flament, C. 2001 *Phys. Rev.* E **63**, 011402.
Hoger, A. 1987 *Intl J. Solids Struct.* **23**, 1645.
Höhler, R., Cohen-Addad, S. & Asnacios, A. 1999 *Europhys. Lett.* **48**, 93.
Höhler, R., Cohen-Addad, S. & Hoballah, H. 1997 *Phys. Rev. Lett.* **79**, 1154.
Jiang, Y., Asipauskas, M., Glazier, J. A., Aubouy, M. & Graner, F. 2000. In *Eurofoam 2000* (ed. P. Zitha, J. Banhart & G. Verbist) p. 297. MIT Verlag, Bremen.
Jiang, Y., Swart, P. J., Saxena, A., Asipauskas, M. & Glazier, J. A. 1999 *Phys. Rev.* E **59**, 5819.
Kabla, A. & Debrégeas, G. 2003 *Phys. Rev. Lett.* **90**, 258303.
Kern, N. & Weaire, D. 2003 *Phil. Mag.* **83**, 2973.
Khan, S. A. & Armstrong, R. C. 1986 *J. Non-Newtonian Fluid Mech.* **22**, 1.
Khan, S. A. & Armstrong, R. C. 1987 *J. Non-Newtonian Fluid Mech.* **25**, 61.
Khan, S. A., Schnepper, C. A. & Armstrong, R. C. 1988 *J. Rheol.* **32**, 69.
Kraynik, A., Reinelt, D. & van Swol, F. 2003 *Phys. Rev.* E **67**, 031403.
Kruyt, N. P. 2003 *Intl J. Solids Struct.* **40**, 511.
Kruyt, N. P. & Rothenburg, L. 1996 *J. Appl. Mech.* **118**, 706.
Kruyt, N. P. & Rothenburg, L. 2002 *Intl J. Solids Struct.* **39**, 311.
Labiausse, V., Höhler, R. & Cohen-Addad, S. 2005 In *Proceedings of Eufoam 2004* (ed. M. Adler). Elsevier (to appear).
Landau, L. D. & Lifschitz, E. M. 1986 *Theory of Elasticity*, 3rd edn. Reed.
Langer, S. A. & Liu, A. J. 1997 *J. Phys. Chem.* B **101**, 8667.
Larson, R. 1997 *J. Rheol.* **41**, 365.
Lauridsen, J., Twardos, M. & Dennin, M. 2002 *Phys. Rev. Lett.* **89**, 098303.
Liao, C. L., Chang, T. P., Young, D. H. & Chang, C. S. 1997 *Intl J. Solids Struct.* **34**, 4087.
Macosko, C. 1994 *Rheology: Principles, Measurements and Applications.* Wiley-VCH.
Mason, T., Bibette, J. & Weitz, D. 1995 *Phys. Rev. Lett.* **75**, 2051.
Mecke, K. & Stoyan, D. (Eds.) 2002 *Morphology of Condensed Matter – Physics and Geometry of Spatially Complex Systems*, Lecture Notes in Physics 600, Proc. of the 2nd conf. 'Spatial Statistics and Statistical Physics', Wuppertal (Germany), March 2001. Springer.
Phan-Thien, N. 2002 *Understanding Viscoelasticity*. Springer.
Porte, G., Berret, J. F. & Harden, J. L. 1997 *J. Phys. II France* **7**, 459.
Poynting, J. H. 1909 *Proc. R. Soc. Lond.* A **82**, 546.
Pratt, E. & Dennin, M. 2003 *Phys. Rev.* E **67**, 051402.
Princen, H. M. 1983 *J. Colloid Interface Sci.* **91**, 160.
Reinelt, D. A. & Kraynik, A. 2000 *J. Rheol.* **44**, 453.
Rosenkilde, C. E. 1967 *J. Math. Phys.* **8**, 84.
Rouyer, F., Cohen-Addad, S., Vignes-Adler, M. & Höhler, R. 2003 *Phys. Rev.* E **67**, 021405.
Tanguy, A., Wittmer, J.-P., Leonforte, F. & Barrat, J.-L. 2002 *Phys. Rev.* B **66**, 174205.
Tanner, R. I. & Tanner, E. 2003 *Rheol. Acta* **42**, 93.
Weaire, D. & Hutzler, S. 1999 *Physics of Foams*. Oxford University Press.
Weaire, D. & Hutzler, S. 2003 *Phil. Mag.* **83**, 2747.
Weaire, D., Kern, N., Cox, S. J., Sullivan, J. M. & Morgan, F. 2004 *Proc. R. Soc. Lond.* A **460**, 569.
Ybert, C. & di Meglio, J.-M. 2002 *C. R. Phys.* **3**, 555.
Zimmerman, J. A. 1999 Continuum and atomistic modeling of dislocation nucleation at a crystal surface ledge. PhD thesis, University of Stanford, chap. 4, pp. 67–106.